Research Square

Preprints are preliminary reports that have not undergone peer review.
They should not be considered conclusive, used to inform clinical practice,
or referenced by the media as validated information.

Simulation of a 16 nm FinFET capacitive biosensor array for label free biological dielectric imaging

Omar Zainelabideen

omarzee@aucegypt.edu

American University in Cairo

Nour Khalil

American University in Cairo

Dalia Eissa

American University in Cairo

Abdullah Elnahhas

American University in Cairo

Mostafa M. Abdelrazik

American University in Cairo

Yehea Ismail

American University in Cairo

Ahmed Saeed

American University in Cairo

Article

Keywords: 16-nm FinFET, capacitive biosensor, ring oscillator, dielectric imaging, CMOS sensor array, multiphysics simulation

Posted Date: November 27th, 2026

DOI: https://doi.org/10.21203/rs.3.rs-11682130/v1

License: This work is licensed under a Creative Commons Attribution 4.0 International License.
Read Full License

Additional Declarations: No competing interests reported.

Simulation of a 16 nm FinFET capacitive biosensor array for label free biological dielectric imaging

Omar Zainelabideen[1]*, Nour Khalil[1], Dalia Eissa[1], Abdullah Elnahhas[1], Mostafa M. Abdelrazik[1], Yehea Ismail[1], and Ahmed Saeed[1]

[1] Electronics and Communications Engineering Department, The American University in Cairo, Cairo, Egypt.

*Corresponding author: Omar Zainelabideen. Email: omarzee@aucegypt.edu.

Abstract

Dense electronic sensor arrays could support rapid, label-free characterization of biological samples, but require compact readout circuits. We present a simulation-based feasibility study of a 16-nm FinFET capacitive biosensor array intended for tissue and cerebrospinal-fluid dielectric imaging. The 16 × 16 array comprises sixteen 4 × 4 subarrays, each sharing a three-stage ring oscillator, with eight 24-bit counters operating in parallel. Multiphysics electrostatic models provide capacitance inputs to post-layout Cadence simulations including extracted interconnect parasitics. The isolated oscillator operates at 3.006 GHz, consumes 2.919 mW, and exhibits 485.7-fs integrated jitter. The integrated readout operates at 1.354 GHz, consumes 8.489 mW, and provides a nominal capacitance sensitivity of 0.805 MHz/fF. An 8 × 8 multiphysics dataset of 72 simulations supports spatial reconstruction and regression-based estimation of the modeled malignant-cell fraction. Ridge regression achieves a held-out test R^2 of 0.9365 and mean absolute error of 0.0704. These results support the architectural feasibility of shared-oscillator dielectric imaging in scaled CMOS. The chip has not been fabricated; experimental validation with calibrated dielectrics and clinically annotated samples is required before diagnostic use.

Keywords: 16-nm FinFET; capacitive biosensor; ring oscillator; dielectric imaging; CMOS sensor array; multiphysics simulation

Introduction

Rapid biological-sample characterization remains a point-of-care challenge. Approximately 20 million new cancer cases are diagnosed annually[1], yet biopsy and conventional histopathology typically require three to ten days[2], trained personnel, and centralized laboratories that are difficult to access in low-resource settings[3]. Cerebrospinal fluid (CSF) analysis likewise relies on biochemical, cytological, and microbiological laboratory testing that may not provide immediate bedside feedback, motivating rapid, low-cost, label-free, and minimally invasive electronic diagnostic-support tools.

Measured dielectric contrast supports label-free sensing: Joines et al. reported frequency-dependent normal/malignant tissue differences from 50 to 900 MHz[4]; later studies separated normal, benign, and malignant breast tissues[5,6] and healthy and malignant colon tissue[7]. CSF also differs strongly from air and may vary with cellular content, proteins, ions, and disease state. Across relevant frequencies, soft tissue and CSF can exhibit effective relative permittivities of approximately $\varepsilon_r = 20\text{-}80$ versus $\varepsilon_r \approx 1$ for air[8,9], enabling a capacitive array to map local dielectric variation.

Complementary metal-oxide-semiconductor (CMOS) capacitive sensing offers low static power, direct digital integration, and reduced labeling or reagent requirements[10,11]. Alhoshany et al. used a low-power successive-approximation capacitance-to-digital readout for the SSAT cancer biomarker[12]; Senevirathna et al. monitored cell proliferation with a lab-on-CMOS capacitance array[13]; Chen et al. used a high-density impedance array for single-cell resolution circulating-tumor-cell counting[14]; Abdelbaset et al. combined a CMOS capacitive matrix, ring-oscillator readout, and Multiphysics-to-circuit simulation to distinguish hepatocellular carcinoma cells from normal liver cells in saline[15]; Krishnan and Levine used time-and frequency-division-multiplexed readout in a 420-pixel ring-oscillator capacitance imager[16]; and Jain et al. combined an in-pixel transimpedance amplifier with a gated ring-oscillator time-to-digital converter for electrochemical impedance spectroscopy, demonstrating DNA hybridization and cardiac-troponin sensing with low phase error and in-pixel averaging[17]. Outside CMOS, Prasanthi et al. numerically validated a functionalized hybrid-dielectric OTFT biosensor for cancer biomarker detection in saliva and serum[18].

Two gaps remain: deeply scaled CMOS has not, to our knowledge, been applied to a tissue-contacting capacitive array, despite its higher ring-oscillator frequencies and potential capacitance-to-frequency gain; and prior CMOS platforms largely target molecular biomarkers or cell suspensions rather than direct dielectric mapping of biopsy tissue or CSF droplets, whose bulk dielectric contrast may enable faster measurements.

Accordingly, this paper presents a 16-nm FinFET capacitive biosensor array intended for label-free dielectric characterization of biopsy tissue and CSF, combining a 16 × 16 array, localized ring-oscillator sharing, 24-bit counter digitization, microcontroller-based map reconstruction, and a Multiphysics-to-post-layout Cadence workflow that maps tissue-dependent capacitance changes to frequency and digital count.

System overview and sensing principle

Proposed point of care workflow

The proposed point-of-care sensing workflow is illustrated in Supplementary Figure S1. A buffer-only reference first compensates for pixel mismatch, parasitic capacitance, and surrounding fluid. A biopsy specimen or CSF droplet then perturbs the fringing fields above the 16 × 16 top-metal electrodes and changes local pixel capacitance.

The selected capacitance shifts a local ring-oscillator frequency that is digitized by a counter; reference subtraction yields a 256-pixel differential dielectric map for reconstruction and classification. The platform is

intended as a rapid screening and characterization aid, not a replacement for histopathology or clinical laboratory diagnosis.

Capacitive dielectric sensing principle

For an ideal capacitor,

$$C = \frac{\varepsilon_0 \varepsilon_r A}{d} \quad (1)$$

where ε_0 is the vacuum permittivity, ε_r is the relative permittivity, A is the effective electrode area, and d is the separation. Although the pixels are dominated by fringing fields, the same principle applies: changes in the effective permittivity of air, buffer, tissue, or cerebrospinal fluid change the measured capacitance. Differences in cellular density, water content, morphology, extracellular structure, and ionic composition therefore form a spatial dielectric signature. Finite-element simulations estimate the capacitance for each sample condition, and the extracted values are applied to circuit-level simulations.

Capacitance to frequency conversion

The capacitive sensor and its ring-oscillator loading configuration are illustrated in Supplementary Figure S2. Each selected pixel loads a three-stage ring oscillator. For an N-stage oscillator,

$$f_{\mathrm{osc}} = \frac{1}{2N t_{\mathrm{d}}} \quad (2)$$

where t_d is the average inverter delay; increased capacitance raises t_d and lowers the oscillation frequency. Femtofarad-scale dielectric changes are therefore converted into measurable frequency shifts.

This compact, digital-friendly conversion avoids a precision analog front end and interfaces directly with dense counter-based readout.

Counter based digital readout

The oscillator is digitized by counting cycles during a fixed window, so capacitance-induced frequency shifts appear directly as digital count changes.

$$N_{\mathrm{count}} = f_{\mathrm{osc}} \times T_{\mathrm{window}} \quad (3)$$

The minimum frequency resolution is

$$\Delta f_{\mathrm{min}} = \frac{1}{T_{\mathrm{window}}} \quad (4)$$

Longer windows improve resolution but increase scan time and sensitivity to sample motion.

A 24-bit counter provides the required dynamic range for GHz-range outputs. The latched counts are mapped to the selected pixels, baseline-subtracted, and reconstructed by the microcontroller.

System architecture

The 256-pixel array is partitioned into sixteen 4 × 4 subarrays sharing one local ring oscillator each, keeping capacitance-sensitive routing short while avoiding a dedicated oscillator per pixel. The subarrays form eight readout pairs; a high-speed 2-to-1 multiplexer in each pair routes one oscillator to a 24-bit counter, so eight pixels are measured in parallel and latched into a 192-bit register per acquisition window. The register is serialized over a 3-bit microcontroller bus; the chip therefore uses 16 ring oscillators, eight multiplexers, eight counters, and one shared decoder while preserving 256-pixel spatial resolution. Figure 1 shows the overall 16 × 16 sensor-array architecture, while Supplementary Figure S3 details the paired readout paths.

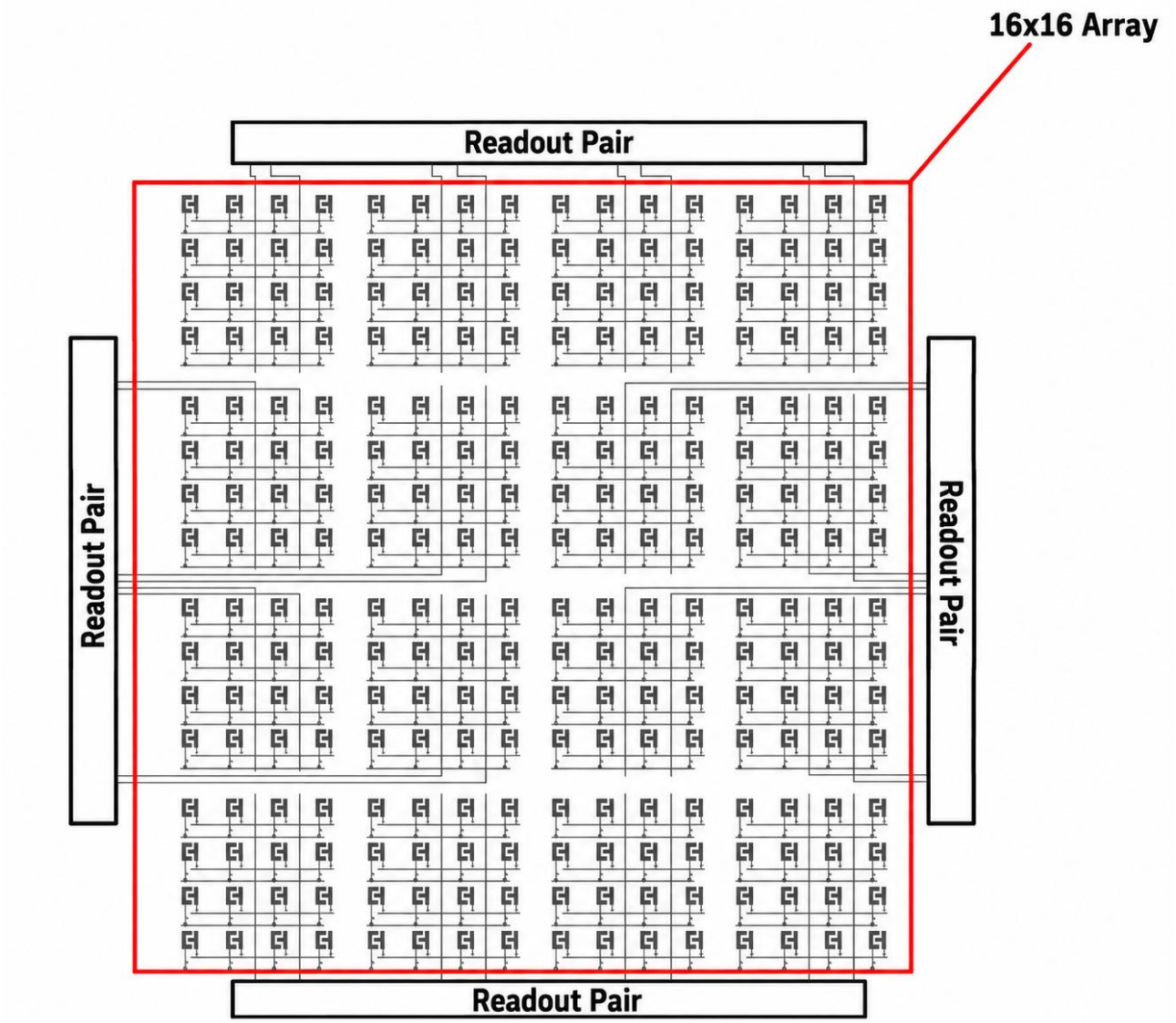


Figure 1. Architecture of the 16 × 16 sensor array. Sixteen local ring oscillators serve sixteen 4 × 4 subarrays, with eight parallel counter channels. The sensor-readout-pair architecture is shown in Supplementary Figure S3.

Capacitive pixel and sensor selection network

Each pixel is a 7 μm × 7 μm Metal-9 electrode, using the uppermost and thickest metal of the 16 nm FinFET process to maximize fringing-field interaction while limiting series resistance and high-frequency interconnect loss. The chip passivation stack or post-fabrication biointerface separates the sample from the metal; its thickness and permittivity are included in the multiphysics model because they directly affect sensitivity.

A shared standard-cell 4-to-16 decoder addresses the pixels.

Each sensor connects to the oscillator at both terminals through complementary NMOS-PMOS transmission gates; the enabled decoder output turns on both switches of the selected pixel, while all others remain isolated to prevent unwanted capacitive loading.

Ring oscillator sensing core

Each 4 × 4 subarray uses a three-stage custom CMOS ring oscillator. Every inverter contains one NMOS and one PMOS with L = 16 nm, W = 250 nm, and n = 16; the selected sensor connects to nodes Cap1 and Cap2, making the effective load the node parasitics plus sensor capacitance. The schematic implementation of the sensing core is shown in Figure 2a.

For a three-stage oscillator, the oscillation frequency is approximately

$$f_{\mathrm{osc}} = \frac{1}{6t_{\mathrm{d}}} \quad (5)$$

Increasing selected capacitance increases the average stage delay and lowers oscillation frequency; decreasing capacitance has the opposite effect, so frequency represents local dielectric loading.

A standard-cell NOT gate, two buffers, and a D flip-Rlop condition the oscillator before the local multiplexer and counter; an additional output buffer provides drive. NMOS-PMOS power gating disables the oscillator when idle to reduce dynamic power and coupling to neighboring circuitry, and the core is replicated once per subarray.

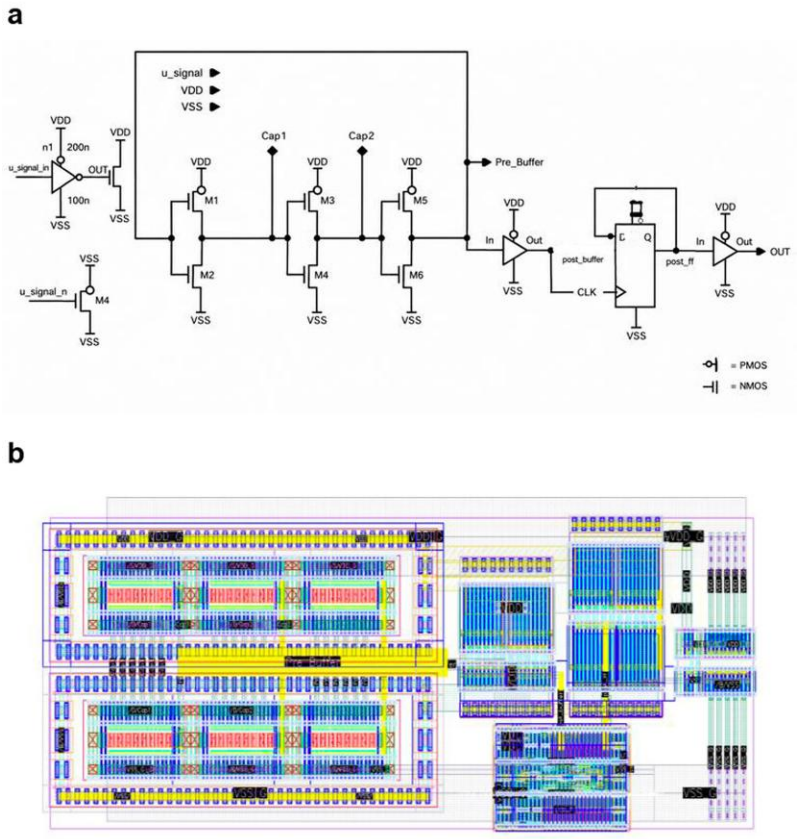


Figure 2. Three-stage ring-oscillator sensing core. (a) Schematic implementation including the sensor-loading nodes and output conditioning. (b) Physical layout of the oscillator core.

Counter and register readout

The selected oscillator frequency is digitized over a fixed measurement interval according to

$$N_{\mathrm{count}} = f_{\mathrm{osc}} \times T_{\mathrm{meas}} \quad (6)$$

The Counter_reg_MUX block combines one 24-bit counter with three 8-bit register-and-multiplexer slices, converting the sensor-induced frequency shift into a stable digital word.

The counter cascades twelve 2-bit sections based on T flipflops with enable/carry logic. Its maximum unsigned count is

$$2^{24} - 1 = 16{,}777{,}215 \quad (7)$$

providing the dynamic range required for GHz-range oscillator measurements. Counter reset and enable signals define the acquisition window and prevent residual counts from carrying into the next measurement. After counting, the lower, middle, and upper 8-bit groups are latched and each feeds a hierarchical 8-to-1 multiplexer for serialization. This retains the full 24-bit resolution without a wide parallel output bus or a separate analog-to-digital converter per pixel.

Control timing and array scan protocol

Full-array acquisition uses the shared 4-to-16 decoder to select one relative pixel position in every subarray and each pairwise 2-to-1 multiplexer to select the oscillator connected to its counter; a settling interval follows each transition. Each state applies the decoder address and multiplexer phase, settles, resets/enables the counters for a fixed window, latches eight 24-bit results, and serializes the 192-bit word. Sixteen decoder positions and two multiplexer phases give 32 states with eight pixels measured per state. The scan time is

$$T_{\text{scan}} = 32[T_{\text{settle}} + T_{\text{meas}} + T_{\text{latch}} + T_{\text{serial}} + T_{\text{overhead}}] \quad (8)$$

For a 5-ms window and approximately 3-GHz maximum oscillator frequency, the largest count is 15×10^6, below the 24-bit limit of 16,777,215 with approximately 11.8% overflow margin; minimum counting time is therefore 160 ms, excluding control and serialization overhead.

Each 192-bit word is sent through the 3-bit bus in 64 steps; the microcontroller maps each 24-bit count to its decoder address and multiplexer phase to reconstruct the full map.

Methods

Simulation software

Circuit simulations were performed using Cadence Virtuoso (IC23.1; Cadence Design Systems, https://www.cadence.com).

Multiphysics simulation

A representative 16-sensor tile of the 16 × 16 array is modeled in a three-dimensional electrostatic domain, with biological buffer as the reference medium around the electrodes; the electric field is solved for each loading condition.

A buffer-only simulation is performed first. Subsequent cases are expressed as differential capacitance,

$$\Delta C = C_{\text{sample}} - C_{\text{buffer}} \quad (9)$$

which suppresses fixed background and parasitic contributions and isolates the dielectric effect of the specimen. Air, buffer, normal breast tissue, and malignant breast tissue are simulated with literature-based permittivities. The software integrates induced electrode surface charge to obtain per-pixel capacitance, and the resulting ΔC values become the circuit-simulation inputs.

Spatial reconstruction and cell localization

After a full scan, the microcontroller reconstructs a differential dielectric map for localization and derives a continuous malignancy index from the same response.

At each pixel, the buffer count is subtracted from the sample count and converted to ΔC. Because frequency falls as capacitive loading rises, the differential count preserves dielectric contrast; the 256 values are corrected for array ordering and reshaped into a 16 × 16 map. The modeled buffer uses $\varepsilon_r = 80$ and normal, benign, and malignant tissue $\varepsilon_r = 45$, 55, and 65, respectively, so each tissue gives negative ΔC relative to buffer: empty pixels remain near zero, malignant pixels form a moderately negative band, and normal/benign pixels shift more negatively. The expected malignant band is determined from the relative contrast between malignant and normal tissue:

$$Contrast\ ratio\ = \frac{15}{35} \approx 0.43 \quad (10)$$

The candidate band is bounded by

$$0.55 \times min(\Delta C) \quad (11)$$

and

$$0.08 \times min(\Delta C) \quad (12)$$

These normalized limits retain malignant candidates while adapting to the strongest response in each scan and rejecting near-zero background and the more negative normal/benign signatures. A 3 × 3 local-minimum filter identifies one representative pixel per malignant footprint, consistent with the approximately 9000-nm cell radius and 7000-nm pixel pitch. Candidates are sorted by ΔC and accepted only when separated by more than 1.8 grid units to prevent double counting adjacent pixels. The retained coordinates and ΔC values are overlaid on the differential heatmap and interpolated contour map to estimate malignant-cell locations.

Regression based malignancy estimation

A parallel regression stage estimates the fraction of malignant cells in the sample rather than making only a binary decision. The target is defined as:

$$malignancy_{\text{index}} = \frac{N_{\text{malignant}}}{N_{\text{benign}} + N_{\text{malignant}}} \quad (13)$$

The index ranges from 0 for fully benign to 1 for fully malignant. Each measurement uses the raw spatial ΔC values plus seven descriptors: mean, standard deviation, maximum, total signal energy, row and column centers of mass, and left-to-right energy ratio.

Because full 16 × 16 dataset generation was computationally expensive, validation used an 8 × 8 array. After serpentine-order correction, each sample produced 64 pixel values plus seven aggregate descriptors, a 71-feature vector; the same feature extraction method applies to the final 256-pixel array.

Ridge Regression is trained after feature standardization using a 75/25 train-test split; five-fold cross-validation assesses stability. A Random Forest with 400 estimators and maximum depth 10 is evaluated as a nonlinear comparison.

Results

Post-layout results are reported for the isolated ring oscillator, integrated sensor-readout chip, and multiphysics/regression pipeline. Unless stated otherwise, circuit results include extracted interconnect resistance and capacitance.Figure 2b shows the three-stage ring-oscillator layout. While the complete sensor-array layout is shown in Figure 3a, as well as the full chip layout with pads in Figure 3b. Supplementary Figure S6 shows the active die area with each functional block labeled.

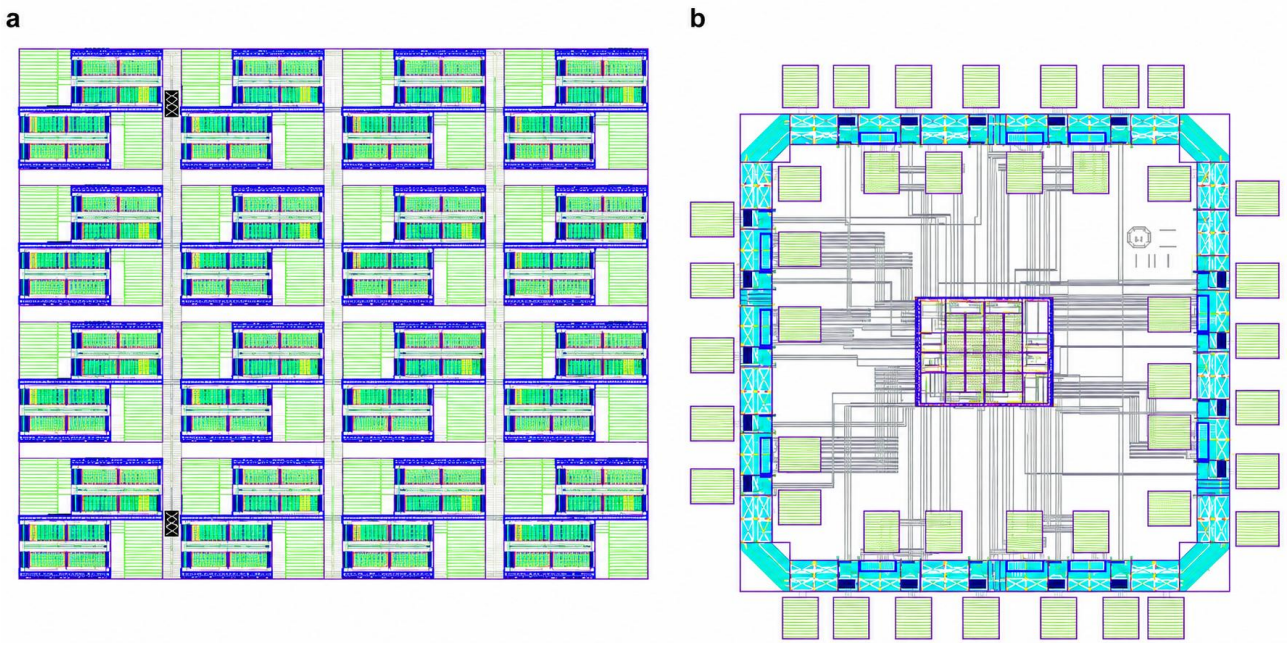


Figure 3. Physical implementation of the sensor and chip. (a) Sensor-array layout. (b) Full-chip layout including the pad frame. Counter/register and repeated-block layouts are provided in Supplementary Figures S4 and S5.

Ring oscillator

Startup steady state and sensitivity

Transient simulation confirms reliable startup and rail-to-rail periodic operation; the extracted frequency is 3.006 GHz and average power 2.919 mW. A load-capacitance sweep gives resolvable small-capacitance frequency shifts and, with an appropriate counter window, supports sub-femtofarad biological sensing resolution.

Periodic steady state analysis

PSS gives a 3.01-GHz fundamental, closely matching the 3.006-GHz transient result and confirming a stable periodic solution. At 50 Ω, the 2.956-dBm first harmonic dominates and higher harmonics are substantially smaller; at 10 kΩ, first harmonic power is -20.05 dBm. Frequency rises monotonically with V_{DD} as inverter delay falls.

Phase noise and jitter analysis

PSS/PNoise gives -64 dBc/Hz at 182.5-kHz offset and -70.64 dBc/Hz at 500 kHz; flicker noise dominates near the carrier and thermal noise at larger offsets. Integrated jitter is 485.7 fs, only 0.146% of the 332.7-ps period at 3.006 GHz.

Harmonic balance and noise analysis

HB converges to a 3.013-GHz fundamental with diminishing higher harmonics. At 50 Ω, the approximately 312-mV output corresponds to 1.947 mW (2.89 dBm), sufficient to drive the following digital stage.

HB noise shows AM/PM noise concentrated near the carrier and decreasing with offset; one extracted phase-noise point is approximately -152 dBc/Hz, and the supply-current spectrum is dominated by the oscillation fundamental.

Sweeping V_{DD} from 0.8 to 1.0 V raises frequency from 3.014 to 3.892 GHz; the tuning slope decreases slightly at the highest voltages, indicating gradual saturation, with a nominal tuning point of approximately 0.7973 V.

Transfer function analysis

The small-signal XF magnitude is approximately -26.5 dB at low-to-mid frequencies, rising to about -24 dB at high frequency mainly from capacitive feedthrough and parasitic coupling, with no strong high-Q resonance. Because the oscillator is nonlinear, XF is supplementary rather than a primary metric.

Process voltage and temperature analysis

Post-layout process-voltage-temperature (PVT) simulations use nominal (0.8 V, 27 °C), slow (0.96 V, 85 °C), and fast (1.05 V, -40 °C) conditions; Table 1 summarizes frequency, power, spectral, noise, and jitter metrics. Frequency and power rise across the nominal, slow, and fast cases (3.006/3.678/4.131 GHz and 2.91/6.10/7.42 mW), reflecting the combined process, supply, and temperature changes rather than process variation alone.

$$P \propto C_{\mathrm{l}} {V_{\mathrm{DD}}}^2 f \quad (14)$$

Consistent with dynamic-power scaling, the fast corner exhibits the highest switching-power consumption. Across the evaluated PVT corners, PSS and HB analyses recover the oscillation fundamental, while phase noise remains near -70 dBc/Hz at the reported offset and jitter remains below 1 ps.

Table 1. Simulated ring-oscillator performance across PVT corners

Metric	Nominal	Slow	Fast
Frequency (GHz)	3.006	3.678	4.131
Power consumption (mW)	2.91	6.10	7.42
PSS output power at 50 Ω (dBm)	2.957	4.496	5.447
PSS fundamental frequency (GHz)	3.01	3.682	4.129
Output noise (dBc/Hz)	-70.41	-71.08	-70.46
JC[k = 10] (fs)	493.3	300.3	262.9
HB output magnitude (mV)	310.6	303.2	318.7
HB output power at 50 Ω (mW)	1.929	1.838	2.031
HB output power at 50 Ω (dBm)	2.854	2.644	3.077
HB fundamental frequency (GHz)	3	3	3
JC RMS (as)	197.9	234.1	139.6

Metric	Nominal	Slow	Fast
JCC RMS (as)	6.42	7.595	4.53
PSS output power at 10 kΩ (dBm)	-20.05	-18.51	-17.56
Tuning parameter (mV)	797.3	787.7	811.7

Conditions: nominal 0.8 V, 27 °C; slow 0.96 V, 85 °C; fast 1.05 V, -40 °C. PSS, periodic steady state; HB, harmonic balance; RMS, root mean square.

Integrated system

The sensor-array and full-chip layouts are shown in Figure 3. Supplementary Figures S4 and S5 show the counter/register layout and the repeated readout block, respectively.

Startup and steady state

End-to-end transient simulation verifies joint oscillator, multiplexer, counter, register, and control operation without disrupting frequency measurement. After approximately 20 ns settling, the system oscillates at 1.354 GHz with 12.93-mA average current, 8.489-mW power, and 0.805-MHz/fF sensitivity; current increases during counter/register switching as expected. The corresponding DC operating-point quantities are summarized in Supplementary Table S1 and system-level transient waveforms are shown in Figure 4a.

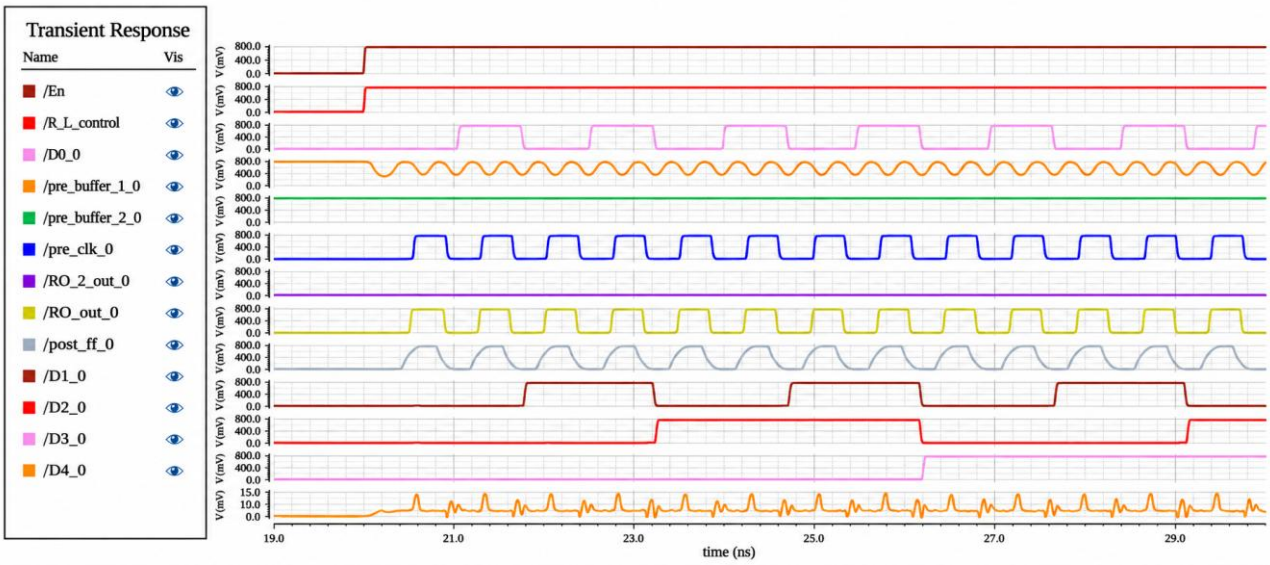


Figure 4. Simulated system-level waveforms giving a time-domain response of control and ring-oscillator signals during sensing and readout.

Periodic steady state and harmonic balance

System-level PSS gives a 1.304-GHz fundamental, close to the 1.354-GHz transient value, confirming periodic operation after full readout loading.

After startup, HB reaches a stable periodic state with an approximately 1.4-GHz fundamental, again close to transient, showing that chip-level loading does not destabilize the counter-useful signal.

Process voltage and temperature analysis

The integrated chip was evaluated at nominal (0.8 V), slow (0.96 V, 85 °C), and fast (1.05 V, -40 °C) conditions; Table 2 reports the extracted metrics. Nominal and slow frequencies are 1.354 and 0.4405 GHz; no fast-corner frequency was extracted in the available simulation set. Transient power is 8.489, 15.02, and 11.52 mW, and average transient voltage is 0.8, 0.7959, and 1.043 V for nominal, slow, and fast cases, respectively. The lower frequency than the isolated oscillator reflects multiplexer, counter, register, control, and routing loads; Table 2 DC voltage entries are measured internal nodes, not the supply rail.

Table 2. Simulated integrated-system performance across PVT corners

Metric	Nominal	Slow	Fast
Frequency (GHz)	1.354	0.4405	Not extracted
Transient power (mW)	8.489	15.02	11.52
Average DC power (mW)	3.2235	24.12	19.35
Average DC node voltage (mV)	1.436	25.74	22.28
Average transient voltage (V)	0.8	0.7959	1.043

Conditions: nominal 0.8 V; slow 0.96 V, 85 °C; fast 1.05 V, -40 °C. The DC voltage values refer to internal nodes rather than the supply rail. No fast-corner frequency was extracted in the reported simulation set.

Multiphysics simulation and malignancy estimation

An 8 × 8 multiphysics campaign was used because a sufficiently large 16 × 16 training set was computationally prohibitive; although prototype geometry changes absolute capacitance, it preserves the differential sensing and processing flow of the final chip.

Reduced array model

The quasi-static model contains 64 electrodes of 7200 × 6753 nm with 0.9-µm separation over an approximately 54 × 57.6-µm sensing area; it retains on-chip serpentine wiring order and models the substrate as air ($\varepsilon_r = 1$). Normal, benign, and malignant cells are modeled as spheres 1500 nm above the electrodes; Supplementary Table S2 lists their respective radii and relative permittivities (4000 nm/45, 6000 nm/55, and 9000 nm/65).

A cell-free baseline is subtracted from each run ($\Delta C = C_{run} - C_{baseline}$) to suppress fixed electrode offsets and isolate modeled-cell dielectric contributions.

Spatial reconstruction

A representative mixed sample contains seven malignant and four benign cells, corresponding to a malignancy index of 0.636. The 64 baseline-subtracted capacitance values range from 38.2 to 172.7 aF, with the largest responses occurring near malignant-cell locations. Reversing every other row of the serpentine-ordered data reconstructs the physical 8 × 8 sensor map.

Regression results

The dataset contains 72 simulations: 18 fully benign, 12 fully malignant and 42 mixed. Each uses 64 pixel-level ΔC values plus seven descriptors (71 features); data were standardized and split 75/25 into training/test sets with random_state = 42.

Ridge Regression and Random Forest use the same 71-feature representation; Random-Forest importance concentrates in pixels with the strongest dielectric contrast, supporting physical relevance of the learned response.

Ridge Regression achieves test MAE = 0.0704 and R^2 = 0.9365; five-fold cross-validation gives MAE = 0.0821 ± 0.0157, with performance assessed on this limited simulated dataset.

Peak localization and regression therefore provide complementary spatial and quantitative outputs. These reduced array results demonstrate feasibility; full-resolution performance requires experimental data from the fabricated 256-pixel chip. The resulting raw differential-capacitance heatmap and detected-peak map are shown in Figure 5a and b, respectively.

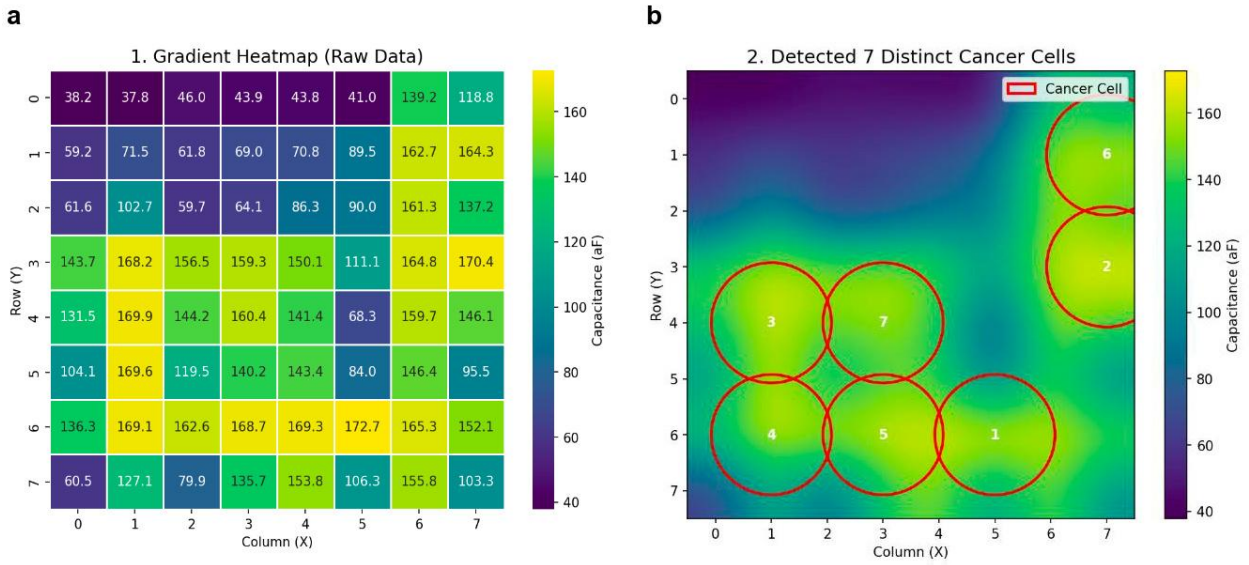


Figure 5. Spatial reconstruction of a representative simulated 8 × 8 sample. (a) Raw differential-capacitance heatmap. (b) Bicubic map with seven detected malignant-cell peaks. A 1.8-grid-unit exclusion distance prevents adjacent detections from being counted twice. The representative sample contains seven modeled malignant cells and four modeled benign cells.

Discussion

Table 3 compares representative CMOS biosensor arrays. Prior systems advance biomarker sensing, cell monitoring, impedance spectroscopy, and capacitance imaging but generally use mature nodes, molecular/cultured-cell targets, or instrumentation-intensive readout; this work targets direct biopsy-tissue and CSF dielectric mapping in 16-nm FinFET CMOS.

Table 3. Comparison of representative CMOS biosensor arrays

Work and implementation	Readout	Target	Reported result
Alhoshany et al.[12] 0.18-µm CMOS; array n.r.	12-bit SAR CDC	SSAT biomarker	4.5-fF resolution; 2.1 µW
Senevirathna et al.[13] 0.35-µm CMOS	C-to-f	Cell proliferation	590 kHz/fF
Chen et al.[14] 0.18-µm CMOS; 96 × 96, 25-µm electrodes	Impedance	CTC counting	Approximately 9000 electrodes

Work and implementation	Readout	Target	Reported result
Abdelbaset et al.[15] 0.13-µm CMOS; 10 × 10	Ring oscillator	Single HCC cells	Multiphysics-to-circuit; saline discrimination
Kilpijärvi et al.[19] CMOS + LTCC; 4 × 4	Ring oscillator	Cell proliferation	57.2-MHz baseline; approximately 1.1-MHz shift
Widdershoven et al.[20] 90-nm CMOS; 256 × 256 nanoelectrodes	HF CBCM / EIS	Label-free imaging	50-70-MHz spectroscopy
Krishnan and Levine[16] 0.18-µm CMOS; 420 pixels	CFC; TDM/FDM	Electrochemical capacitance imaging	5-180-MHz CFC; TDM/FDM
Jain et al.[17] 0.18-µm CMOS; 16 × 20	Phase-only EIS + RO TDC	DNA / troponin	0.035% RMS phase error at 100 kHz
Lai et al.[21] 0.18-µm CMOS; 480 × 960, 2.25-µm pixels	Time-sharing TDC	Life-science imaging	43 fps; 6.896 codes/fF
This work **16-nm FinFET; 16 × 16, 7 × 7-µm pixels**	**Local RO + 24-bit counters**	**Intended tissue / CSF imaging**	**Simulated: 1.354 GHz; 0.805 MHz/fF; 8.489 mW; 160-ms nominal minimum count time**

n.r., not reported; SAR, successive approximation register; CDC, capacitance-to-digital converter; C-to-f/CFC, capacitance-to-frequency conversion/converter; CTC, circulating tumor cell; HCC, hepatocellular carcinoma; LTCC, low-temperature co-fired ceramic; HF, high frequency; CBCM, charge-based capacitance measurement; EIS, electrical impedance spectroscopy; TDM/FDM, time-/frequency-division multiplexing; RO, ring oscillator; TDC, time-to-digital converter; RMS, root mean square; CSF, cerebrospinal fluid; SSAT, spermidine/spermine N^1-acetyltransferase. Results from different studies reflect their respective test conditions and validation methods.

The key architectural contribution is local oscillator sharing: sixteen 4 × 4 subarrays keep sensor interconnects short to limit parasitics and mismatch while reducing 256 potential oscillator-counter channels to 16 oscillators and eight counters without sacrificing the 256-pixel map.

Unlike the biomarker-specific platform reported by Alhoshany et al.[12], this sensor requires no antibody or enzyme functionalization; it targets rapid tissue/CSF mapping rather than long-term proliferation monitoring[13,19] and uses local capacitance-to-frequency conversion instead of high-frequency impedance or large-scale TDC imaging[14,20,21].

Abdelbaset et al.[15] are the closest prior work, but their 10 × 10 mature-CMOS matrix focused on individual cells in saline, whereas this tapeout-ready design targets bulk tissue and CSF with a 16 × 16 FinFET array and full post-layout chip simulation.

Its novelty is the combination of small top-metal pixels, localized oscillator sharing, dense selection routing, 24-bit counter digitization, and post-layout 16-nm implementation for tissue/CSF classification. Current Multiphysics and circuit simulation validation establishes architectural feasibility, not clinical performance.

The packaged chip will then be tested with buffer solutions, dielectric liquids, tissue-mimicking phantoms, biopsy tissue, and CSF droplets. Comparison with Multiphysics/SPICE will validate the co-simulation flow, followed by clinically annotated samples to assess separation of normal, benign, malignant, and abnormal-fluid signatures.

The reported classification outputs concern simulated cell mixtures in a reduced array. They do not establish diagnostic performance in biopsy specimens or cerebrospinal fluid. The present study contains no fabricated-chip measurements, and the relationship between the reduced model and the intended sample environment requires experimental validation.

Conclusion

This work demonstrates the architectural feasibility of a 16-nm FinFET 256-pixel capacitive biosensor for label-free biopsy tissue and CSF dielectric mapping. Local oscillator sharing preserves spatial resolution with 16 oscillators and eight counters while limiting sensitive routing. The isolated oscillator achieves 3.006 GHz, 2.919 mW, and 485.7-fs integrated jitter; the complete post-layout chip achieves 1.354 GHz, 8.489 mW, and 0.805 MHz/fF sensitivity. On the reduced 8 × 8 multiphysics dataset, Ridge Regression achieves MAE = 0.0704 and $R^2 = 0.9365$. Fabrication and testing with calibrated dielectrics and clinically annotated samples remain necessary to establish robustness and diagnostic utility.

Data availability

The datasets generated and/or analysed during the current study are available in the 16nm-FinFet-Ring-Oscillator-Capacitive-Biosensor-Array-for-Label-free-Cancer-Tissue-and-CSF repository, https://github.com/nourwaleedmo/16nm-FinFet-Ring-Oscillator-Capacitive-Biosensor-Array-for-Label-free-Cancer-Tissue-and-CSF-.git

References

1. Bray, F. et al. Global cancer statistics 2022: GLOBOCAN estimates of incidence and mortality worldwide for 36 cancers in 185 countries. *CA Cancer J. Clin.* **74,** 229-263 (2024). https://doi.org/10.3322/caac.21834

2. Volmar, K. E., Idowu, M. O., Souers, R. J., Karcher, D. S. & Nakhleh, R. E. Turnaround time for large or complex specimens in surgical pathology: A College of American Pathologists Q-Probes study of 56 institutions. *Arch. Pathol. Lab. Med.* **139,** 171-177 (2015). https://doi.org/10.5858/arpa.2013-0671-CP

3. Masamba, L. P., Mtonga, P. E., Kalilani Phiri, L. & Bychkovsky, B. L. Cancer pathology turnaround time at Queen Elizabeth Central Hospital, the largest referral center in Malawi for oncology patients. *J. Glob. Oncol.* **3,** 734-739 (2017). https://doi.org/10.1200/JGO.2015.000257

4. Joines, W. T., Zhang, Y., Li, C. & Jirtle, R. L. The measured electrical properties of normal and malignant human tissues from 50 to 900 MHz. *Med. Phys.* **21,** 547-550 (1994). https://doi.org/10.1118/1.597312

5. Lazebnik, M. et al. A large-scale study of the ultrawideband microwave dielectric properties of normal, benign and malignant breast tissues obtained from cancer surgeries. *Phys. Med. Biol.* **52,** 6093-6115 (2007). https://doi.org/10.1088/0031-9155/52/20/002

6. Cheng, Y. & Fu, M. Dielectric properties for non-invasive detection of normal, benign, and malignant breast tissues using microwave theories. *Thorac. Cancer* **9,** 459-465 (2018). https://doi.org/10.1111/1759-7714.12605

7. Fornes-Leal, A., Garcia-Pardo, C., Frasson, M., Pons Beltrán, V. & Cardona, N. Dielectric characterization of healthy and malignant colon tissues in the 0.5–18 GHz frequency band. *Phys. Med. Biol.* **61,** 7334-7346 (2016). https://doi.org/10.1088/0031-9155/61/20/7334

8. Gabriel, S., Lau, R. W. & Gabriel, C. The dielectric properties of biological tissues: II. Measurements in the frequency range 10 Hz to 20 GHz. *Phys. Med. Biol.* **41,** 2251-2269 (1996). https://doi.org/10.1088/0031-9155/41/11/002

9. NIREMF. Dielectric properties of body tissues. http://niremf.ifac.cnr.it/tissprop/ (accessed 2026).

10. Lei, K.-M., Mak, P.-I., Law, M.-K. & Martins, R. P. CMOS biosensors for in vitro diagnosis – transducing mechanisms and applications. *Lab Chip* **16,** 3664-3681 (2016). https://doi.org/10.1039/C6LC01002D

11. Forouhi, S., Dehghani, R. & Ghafar-Zadeh, E. CMOS based capacitive sensors for life science applications: A review. *Sens. Actuators A Phys.* **297,** 111531 (2019). https://doi.org/10.1016/j.sna.2019.111531

12. Alhoshany, A., Sivashankar, S., Mashraei, Y., Omran, H. & Salama, K. N. A biosensor-CMOS platform and integrated readout circuit in 0.18-µm CMOS technology for cancer biomarker detection. *Sensors* **17,** 1942 (2017). https://doi.org/10.3390/s17091942

13. Senevirathna, B. P. et al. Real-time measurements of cell proliferation using a lab-on-CMOS capacitance sensor array. *IEEE Trans. Biomed. Circuits Syst.* **12,** 510-520 (2018). https://doi.org/10.1109/TBCAS.2018.2821060

14. Chen, Y. et al. CMOS high density electrical impedance biosensor array for tumor cell detection. *Sens. Actuators B Chem.* **173,** 903-907 (2012). https://doi.org/10.1016/j.snb.2012.07.024

15. Abdelbaset, R., El-Sehrawy, Y., Morsy, O. E., Ghallab, Y. H. & Ismail, Y. CMOS based capacitive sensor matrix for characterizing and tracking of biological cells. *Sci. Rep.* **12,** 13839 (2022). https://doi.org/10.1038/s41598-022-18005-1

16. Krishnan, A. & Levine, P. M. CMOS ring-oscillator-based electrochemical capacitance imager with frequency-division-multiplexed readout. In *2022 IEEE International Symposium on Circuits and Systems (ISCAS)* 1082-1086 (2022). https://doi.org/10.1109/ISCAS48785.2022.9937308

17. Jain, A., Chung, S., Spencer, E. A. & Hall, D. A. An electrochemical CMOS biosensor array using phase-only modulation with 0.035% phase error and in-pixel averaging. *IEEE Trans. Biomed. Circuits Syst.* **19,** 416-427 (2025). https://doi.org/10.1109/TBCAS.2024.3450843

18. Prasanthi, L. et al. Advanced hybrid dielectric OTFT biosensor for early breast cancer diagnosis with enhanced sensitivity. *Results Eng.* **27,** 107037 (2025). https://doi.org/10.1016/j.rineng.2025.107037

19. Kilpijärvi, J. et al. LTCC packaged ring oscillator based sensor for evaluation of cell proliferation. *Sensors* **18,** 3346 (2018). https://doi.org/10.3390/s18103346

20. Widdershoven, F. et al. A CMOS pixelated nanocapacitor biosensor platform for high-frequency impedance spectroscopy and imaging. *IEEE Trans. Biomed. Circuits Syst.* **12,** 1369-1382 (2018). https://doi.org/10.1109/TBCAS.2018.2861558

21. Lai, L.-H. et al. A 460,800 pixels CMOS capacitive sensor array with programmable fusion pixels and noise canceling for life science applications. *IEEE Trans. Circuits Syst. II Express Briefs* **70,** 1734-1738 (2023). https://doi.org/10.1109/TCSII.2023.3261445

Acknowledgements

The authors acknowledge the support of AP-RIC Office Strategic Initiatives at The American University in Cairo.

Funding

This work was supported by The American University in Cairo through the Bartlett Fund for Critical Challenges (AP-RIC Office Strategic Initiatives).

Author contributions

Omar Zainelabideen performed circuit design and all circuit layout. Nour Khalil and Dalia Eissa contributed to the circuit design. Dalia Eissa performed most of the Multiphysics modeling and diagram drawing, with additional Multiphysics modeling by Abdullah Elnahhas. Abdullah Elnahhas performed the machine-learning work. Mostafa M. Abdelrazik designed the bond pads, handled the tape-out submission and contributed to manuscript drafting. All authors contributed to drafting this paper. Ahmed Saeed co-supervised the research. Yehea Ismail supervised the research.

Additional information

Competing interests

The authors declare no competing interests.

Ethics declarations

This study involved computer simulations using published material parameters and did not involve human participants, human biological samples or animals. Ethics approval and informed consent were therefore not applicable.

Supplementary information

The Supplementary Information contains six supplementary figures and two supplementary tables.

Supplementary Files

This is a list of supplementary files associated with this preprint. Click to download.

- SupplementaryMaterial.zip